ARTICLE

Rationalizing Inter- and Intracrystal Heterogeneities in Dealuminated Acid Mordenite Zeolites by Stimulated Raman Scattering Microscopy Correlated with Super-resolution Fluorescence Microscopy

Kuan-Lin Liu,[*,†,§] Alexey V. Kubarev,[‡,§] Jordi Van Loon,[‡] Hiroshi Uji-i,[†] Dirk E. De Vos,[‡] Johan Hofkens,[†] and Maarten B. J. Roeffaers[*,‡]

[†]Department of Chemistry, Faculty of Sciences, KU Leuven, 3001 Heverlee, Belgium and [‡]Centre for Surface Chemistry and Catalysis, Faculty of Bioscience Engineering, KU Leuven, 3001 Heverlee, Belgium. [§]These authors contributed equally to this work.

ABSTRACT Dealuminated zeolites are widely used acid catalysts in research and the chemical industry. Bulk-level studies have revealed that the improved catalytic performance results from an enhanced molecular transport as well as from changes in the active sites. However, fully exploiting this information in rational catalyst design still requires insight in the intricate interplay between both. Here we introduce fluorescence and stimulated Raman scattering microscopy to quantify subcrystal reactivity as well as acid site distribution and to probe site accessibility in the set of individual mordenite zeolites. Dealumination effectively introduces significant heterogeneities between different particles and even within individual crystals. Besides enabling direct rationalization of the nanoscale catalytic performance, these observations reveal valuable information on the industrial dealumination process itself.

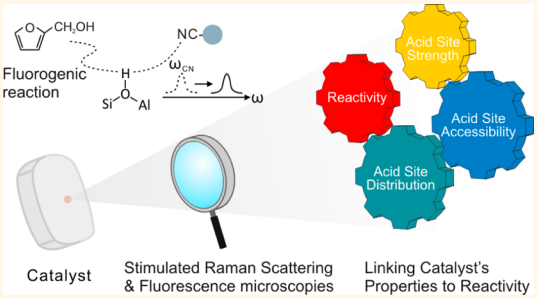

KEYWORDS: dealumination · mordenite · single-molecule microscopy · stimulated Raman scattering · super-resolution fluorescence microscopy · Raman microscopy

Zeolites are porous crystalline solids with pores of molecular dimensions, providing size and shape selectivity in catalysis.[1−4] Acid mordenites (H-MORs) are typical catalysts used in the petrochemical industry, mostly for cracking, isomerization, and alkylation reactions. The Brønsted acidic framework hydroxyls are lining the porous network that consists of main channels (6.5 × 7.0 Å^2) and small channels (5.7 × 2.6 Å^2) oriented along the crystallographic *c*-axis with side pockets (3.4 × 4.8 Å^2) along the *b*-axis. The side pockets are too small for most organic molecules, resulting in a quasi-unidirectional microporous system that makes as-synthesized H-MOR susceptible to mass transport limitations and rapid deactivation.[5,6] Optimization of the catalytic performance often relies on postsynthetic treatments such as dealumination that reduces the framework aluminum content and also introduces mesoporosity, thus enhancing molecular transport and slowing the deactivation by coke formation. Typically, dealumination involves repeated chemical (*e.g.*, acid leaching) and hydrothermal (steaming) treatments that have complex implications on both compositional and structural properties, such as acid site density, accessibility, pore network, *etc.*[7,8] Currently, optimization of H-MOR performance and of catalysts in general is largely based on trial-and-error experiments using bulk catalyst samples, without much insight at the relevant length scales since tools capable of looking beyond the crystal surface

* Address correspondence to maarten.roeffaers@biw.kuleuven.be (M.B.J.R.), d927429@alumni.nthu.edu.tw (K.-L.L.).

Received for review September 30, 2014 and accepted November 17, 2014.

Published online November 17, 2014
10.1021/nn505576p

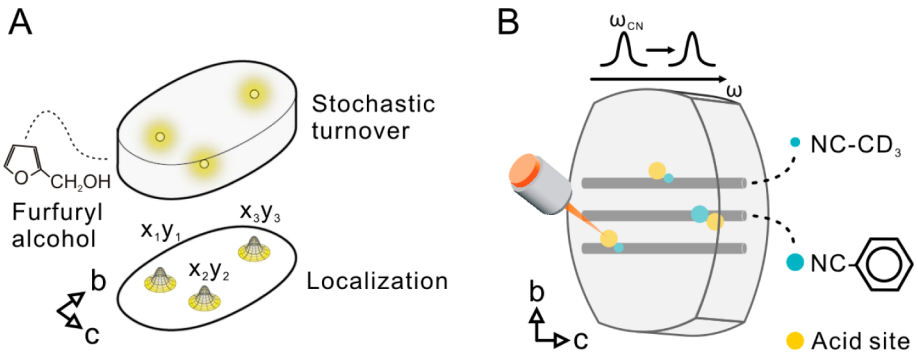

Figure 1. Schematic representation of the used optical micro(spectro)scopic assay. (A) NASCA and (B) SRS microscopy.

and providing relevant information with high sensitivity and spatial resolution are not available.[9−11]

Recently, 3D nanoscale reactivity mapping of catalytic reactions in zeolite catalysts has become possible *via* single-molecule spectroscopy.[12] Nanometer Accuracy by Stochastic Chemical reActions (NASCA) microscopy captures single catalytic conversions of fluorogenic molecules and determination of the local nanoscale reactivity results from accurate fitting and mapping of the recorded emission from individual fluorescent reaction products.[13,14] In depth rationalization of this spatially resolved catalytic performance information was so far not possible because of a lack of complementary techniques in the current catalyst characterization toolbox. Highly specialized scanning transmission X-ray microscopy (STXM) has been proven to generate very detailed chemical composition maps;[15] it provides information on local aluminum content and its coordination in dealuminated zeolites, allowing a rationalization of catalytic performance.[16,17] Moreover, chemical maps obtained from STXM are not limited to aluminum, but they also allow measuring spatial distribution of the other elements, such as carbon in probe molecules, allowing investigation of the acid sites.[18] Infrared spectroscopy using organic probe molecules is routinely applied to characterize acid zeolites, as well, but this technique does not offer the required 3D spatial resolution.[19] Closely related Raman microscopy offers this resolution, but it is much less used because of the strongly interfering background fluorescence and because of the inherently weak signals.[20,21] Various enhancement methods have been developed for Raman spectroscopy over the years, of which coherent Raman scattering seems to offer most advantages for 3D catalyst characterization. As an example, coherent anti-Stokes scattering (CARS) microspectroscopy has been applied to record the density map of thiophene in individual H-ZSM-5 crystals[22] and to follow the catalytic conversion of alkene and glycol in single H-Beta crystals, which provides one with important insights about catalysis, such as reaction pathways and activation energy.[23] However, the nonresonant background inherently distorts the CARS spectrum, requiring complex mathematical treatments to extract quantitative information.[24] The development of stimulated Raman scattering (SRS) microscopy offers an unprecedented capability of fast molecular imaging.[25,26] Unlike the more often used CARS, the SRS signal is free from nonresonant background, thus enabling straightforward quantitative and qualitative analyses without assumptions and data interpretation. Here we show how the complex inter- and intraparticle heterogeneities in catalytic performance observed for dealuminated H-MOR in NASCA microscopy (Figure 1A) can be rationalized by local acid site density and accessibility obtained from SRS microscopy using nitrile probes (Figure 1B). The described method is straightforward and can be widely used in heterogeneous catalysis.

RESULTS AND DISCUSSION

Three synthetic mordenite samples with typical crystal dimensions of 5−10 μm were used in the present study; the parent small-port mordenite has a bulk Si/Al = 6.2 (SP-MOR);[8,27−30] starting from this material, the two other mordenite samples are produced *via* mild (Si/Al = 11; mildly dealuminated MD-MOR) and strong (Si/Al = 65; strongly dealuminated SD-MOR) dealumination by one of several cycles of steaming and subsequent acid leaching as described by Hamon *et al.*[31]

NASCA Microscopy. To investigate the effect of the dealumination process on the catalytic performance at the individual crystal level, NASCA microscopy with furfuryl alcohol (FFA) as a fluorogenic reactant was chosen (Figure 1A); based on the crystal structure of mordenite, FFA fits inside the micropores.[13,32−34] Figure 2A reveals that the catalytic activity of non-dealuminated SP-MOR is limited to the outer surface of the crystal. This is visual evidence of the so-called small-port behavior hindering access of FFA to the microporous network, which was already demonstrated at the bulk level for many synthetic and natural mordenites.[27,28] In addition to this direct visual observation, quantitative analysis of the local reaction rate determined for 500 × 500 × 800 nm^3 voxels (see Supporting Information) reveals a clear bimodal distribution for the presented SP-MOR crystal with active

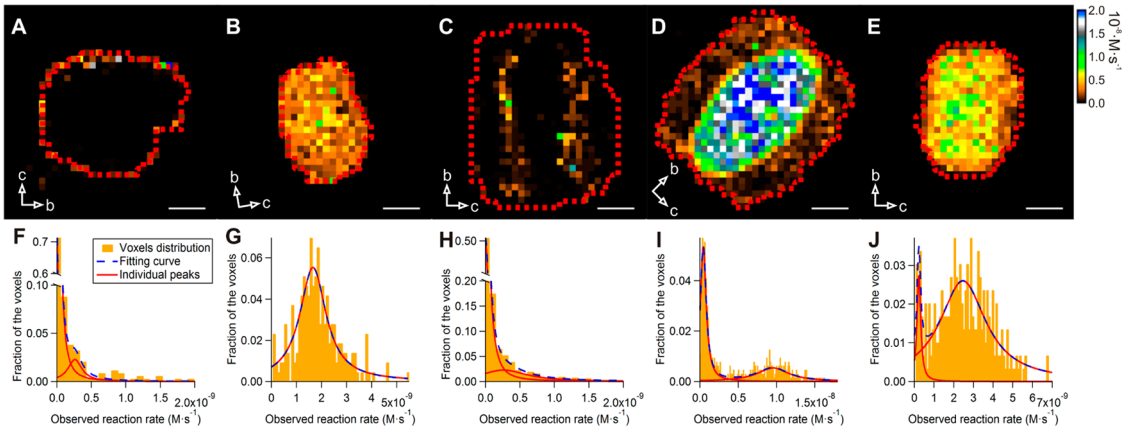

Figure 2. Quantitative analysis of NASCA reactivity maps obtained for 500 × 500 × 800 nm^3 voxels (XYZ). (A) SP-MOR crystal; (B) SD-MOR crystal; (C−E) MD-MOR crystals at different stages of dealumination. Red dashed line indicates the region used for histogram analysis; false color scale indicates observed reaction rate (from 0 to 2 × 10^{-8} M·s^{-1}); crystal axes are indicated by arrows; scale bar: 3 μm. (F−J) Histograms of measured reactivity fitted with single, double, or triple Lorentzian curve as dashed blue line (for parameters, see Table S1): (F) SP-MOR crystal (presented in A); (G) SD-MOR crystal (presented in B); (H) MD-MOR crystal (presented in C); (I) MD-MOR crystal (presented in D); (J) MD-MOR crystal (presented in E).

regions at the crystal periphery that have an activity of 2.6 ± 0.1 × 10^{-10} M·s^{-1}, whereas parts of the crystal away from the surface have no measurable catalytic activity (Figure 2F). Within measured 14 crystals from this batch, no substantial variation in catalytic performance is found. Compared to SP-MOR, severely dealuminated SD-MOR crystals (n = 27) are fully accessible for furfuryl alcohol, showing a homogeneous activity of 16.6 ± 0.4 × 10^{-10} M·s^{-1} throughout the whole crystal volume (Figure 2B,G). The presence of only one peak in the activity histogram, at least at the scale of analysis which is 500 × 500 × 800 nm^3, reflects an efficient pore opening by the dealumination process, that is, transition to large-port mordenite for the whole crystal volume.[35] Surprisingly, and in contrast to SP-MOR and SD-MOR, crystals from the mildly dealuminated MD-MOR sample show a pronounced intercrystal heterogeneity in their reactivity distribution; the crystals from this sample can be divided into three types. About 33% of the crystals (n = 38) display some activity at the outer region of the crystal (2.6 ± 0.6 × 10^{-10} M·s^{-1}) and no catalytic activity at the crystals' center (Figure 2C,H). A second group (25%, n = 29) displays the inverse behavior with a highly active core (95 ± 3 × 10^{-10} M·s^{-1}) and a zone of about 3 μm at the periphery of the crystals with a much lower activity of 4.3 ± 0.1 × 10^{-10} M·s^{-1} (Figure 2D,I). Thirty-three crystals in MD-MOR (28%) show a transitional behavior between crystals in the just described second group and those with homogeneous reactivity observed in SD-MOR as these crystals still show a bimodal activity distribution (Figure 2E,J) with peak positions at 2.3 ± 0.2 × 10^{-10} for the periphery and 24 ± 1 × 10^{-10} M·s^{-1} for the center, but the difference in catalytic activity between the peaks is, however, significantly smaller than for the second group. Finally, 14% (n = 16) of the crystals show transitional behaviors between the aforementioned groups and, therefore, were not assigned to one of them.

Stimulated Raman Scattering Microscopy. The remarkable heterogeneities in reactivity observed in the NASCA experiments are the result of acid site distribution as well as of the molecular accessibility. Since none of the classical characterization tools allows studying these zeolite properties at the relevant subcrystal level, we resort to highly sensitive and spatially resolved chemical imaging by stimulated Raman scattering (SRS) microscopy in combination with nitrile probes (Figure 1B). Bulk infrared spectroscopy has shown that small d-acetonitrile (CD_3CN) molecules effectively access all Brønsted acid sites in both small- and large-port H-mordenites, whereas the bulkier benzonitrile (PhCN) allows discrimination of large-port from small-port behavior.[35−37] Figure 3 presents the density map of adsorbed CD_3CN in three H-MOR samples, obtained from chemical mapping as well as spectral analyses (see below).

Inside SP-MOR crystals (Figure 3A), CD_3CN is distributed homogeneously and the C≡N stretch is shifted by 10 cm^{-1} to 2275 cm^{-1} as compared to liquid CD_3CN (Figure 4A). To gain insight into the orientation of adsorbed nitriles, the polarization dependence of the SRS response was examined. Figure 4B,C depicts the relative C≡N stretch intensity at 2275 cm^{-1} of CD_3CN adsorbed in the SP-MOR along the crystallographic ac and bc planes as a function of angle θ between laser polarization and the crystallographic b-axis. A uniaxial symmetry is observed with the signal about 2.3 times higher when the lasers are polarized in the crystallographic b-axis than in either the a- or c-axis, indicating that a fraction of nitriles is symmetrically oriented with respect to the crystallographic b-axis. These polar plots can be simulated by a sum of two components, an isotropic (circle) and an anisotropic component (cos^2 θ),

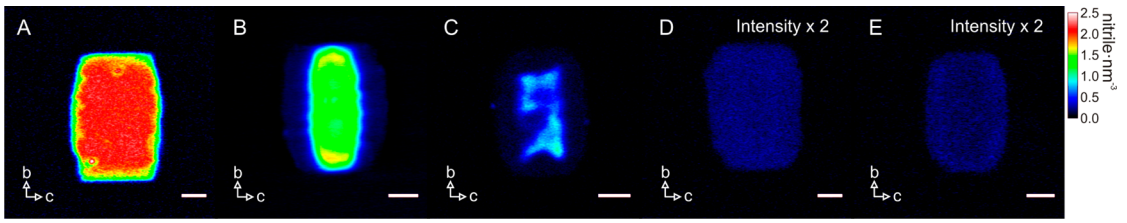

Figure 3. Chemical mapping of CD_3CN adsorbed in H-MORs. (A) SP-MOR; (B−D) MD-MOR crystals at different stages of dealumination: (B) early, (C) intermediate, and (D) late stages; (E) SD-MOR. False color scale indicates the acid site density (from 0 to 2.5 nitrile·nm^{-3} for A−C and from 0 to 1.25 nitrile·nm^{-3} for D,E); crystal axes are indicated by arrows; scale bar: 3 μm.

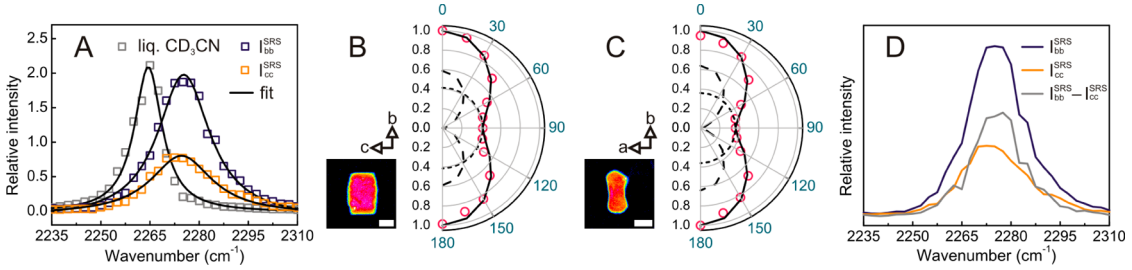

Figure 4. SRS microspectroscopy and polarization dependence of CD_3CN adsorbed in SP-MOR. (A) SRS response of the C≡N stretch region of liquid CD_3CN (×0.2) and of CD_3CN adsorbed in SP-MOR (averaged over a whole crystal) recorded with lasers polarized in crystallographic *b*- (I_{bb}^{SRS}) and *c*-axes (I_{cc}^{SRS}); spectra are fitted by a single Lorentzian curve (solid line). (B,C) Polar plot for C≡N stretch (2275 cm^{-1}) in SP-MOR crystals with different crystal orientations shown in the insets as a function of θ (angle between laser polarization and crystallographic *b*-axis); the polar plots can be simulated by the sum (solid line) of a $\cos^2\theta$ function (anisotropic component, dashed line) and a circle (isotropic component, dotted line); scale bar: 5 μm. (D) Spectra for the anisotropic ($I_{bb}^{SRS} - I_{cc}^{SRS}$) and the isotropic ($I_{cc}^{SRS}$) components in the C≡N vibration.

with the latter oriented along the crystallographic *b*-axis (Figure S1). Theoretical calculation by Dominguez-Soria *et al.* suggested that part of the CH_3CN adsorbed in H-MOR is confined in the side pocket, with its C≡N bond parallel to the crystallographic *b*-axis, to access acid sites in the side pockets; CD_3CN molecules are tilted and become rather randomly distributed to interact with acid sites in the 12-membered ring channels.[38] Therefore, the anisotropic and isotropic components can be assigned to CD_3CN interacting with acid sites in the side pocket and main channel, respectively. Here we introduce I_{kl}^{SRS} to denote the SRS response obtained with pump and Stokes beams polarized in the *k* and *l* directions, respectively. When both lasers are polarized along the *a* or *c*-axis, only the isotropic component contributes to SRS response (I_{cc}^{SRS} or I_{aa}^{SRS}), whereas both components are present with lasers polarized along the crystallographic *b*-axis (I_{bb}^{SRS}). The spectral response of CD_3CN interacting with acid sites in the side pocket, approximated by $I_{bb}^{SRS} - I_{cc}^{SRS}$, is similar to that of CD_3CN in the main channel (Figure 4D).

Taking advantage of the linear concentration dependence of the SRS signal, one can evaluate the absolute local density of adsorbed CD_3CN by comparing its signal intensity with that of liquid CD_3CN with known molecular density (10.8 nm^{-3}). In contrast to the isotropic distribution of CD_3CN in the main channels, the highly oriented CD_3CN in the side pockets leads to a uniaxial symmetry of the SRS response in the focal volume. The measured intensity thus contains mixed information about oscillator density and molecular orientation. An orientation-independent Raman spectrum of adsorbed CD_3CN should be obtained before quantitatively comparing the integrated C≡N stretch intensity with its liquid counterpart. In brief, the orientation-independent spectrum can be obtained from a linear combination of two SRS spectra recorded with lasers polarized along the crystallographic *b*- and *c*-axes and normalized for the laser power (detailed information on the local CD_3CN quantification can be found in the Supporting Information). Similarly, the nitrile density map can be reconstructed using a linear combination of two single-frequency SRS images recorded at the peak of the C≡N stretch along the crystallographic *b*- and *c*-axes. The resulting chemical map (Figure 3) is orientation-independent, assuming constant bandwidth, and after laser power normalization, the scale is calibrated with that of liquid CD_3CN.

For the investigated SP-MOR crystals (n = 19), an average density of 1.81 ± 0.11 nm^{-3} was found matching the expected framework aluminum density. Since the SRS response can be decomposed in an isotropic component (I_{cc}^{SRS}) and an anisotropic component ($I_{bb}^{SRS} - I_{cc}^{SRS}$) representing CD_3CN interacting with acid sites in the main channel and in the side pocket, respectively, the integrated spectral peak intensity reveals their relative abundance in a single-crystal or subcrystal region (see Supporting Information). For SP-MOR, a ratio of 0.37 ± 0.05 can be calculated, which

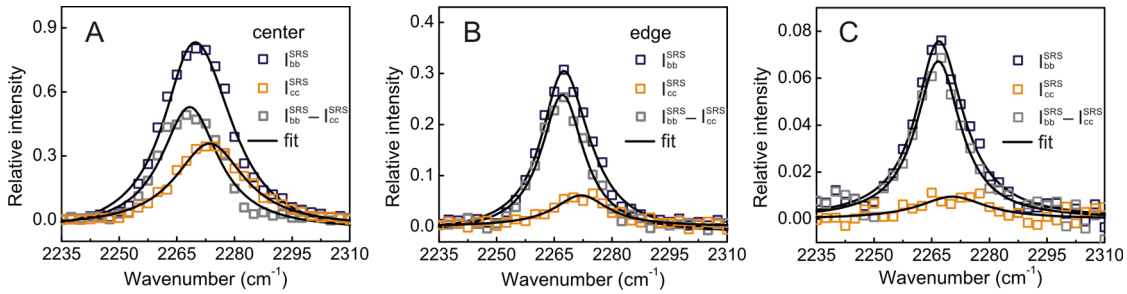

Figure 5. SRS microspectroscopy of CD_3CN adsorbed in MD-MOR and SD-MOR. SRS spectra of CD_3CN adsorbed in the (A) center and (B) edge of an early dealuminated MD-MOR crystal and (C) in the SD-MOR recorded with lasers polarized in crystallographic *b*- (I_{bb}^{SRS}) and *c*-axes (I_{cc}^{SRS}).

is similar to the 1:3 ratio recently reported by Huo *et al.* based on bulk NMR spectroscopy.[39]

For MD-MOR, with an average acid site density of 0.31 nm^{-3} (total = 13), heterogeneous acid site distributions within individual particles and varying total acid site densities among different crystals are observed (Figure 3B–D). Based on the total acid site density per crystal, a significant intraparticle heterogeneity is uncovered for the first time; similar to the NASCA results, crystals can be divided into three groups representing a gradual transition from SP-MOR toward SD-MOR behavior: early (>0.40 nm^{-3}), intermediate (0.40–0.15 nm^{-3}), and late stage (<0.15 nm^{-3}) of dealumination. For early stage dealuminated crystals (n = 4), acid site densities at the center of the crystal are 0.78–1.15 nm^{-3} and there is a zone with an acid site density of 0.15–0.17 nm^{-3} underlying the crystal facet where the main channels are surfacing (Figure 3B). For the intermediate stage dealuminated crystals (n = 5), the behavior is similar; however, the absolute densities in the center (0.25–0.99 nm^{-3}) and at the edge (0.10–0.15 nm^{-3}) are generally lower (Figure 3C). Crystals at the late dealumination stage (n = 4) in this sample show homogeneous distributions with densities of 0.08–0.11 nm^{-3} (Figure 3D). Further dealumination also results in homogeneous distribution of the acid site with lower density (0.07–0.1 nm^{-3}) in SD-MOR (n = 3, Figure 2E). Most crystals (n = 47), however, did not show a measurable SRS signal while the detection limit of our current setup was determined to be 0.07 molecules nm^{-3} with a signal-to-noise ratio larger than 3. Whereas the Si/Al ratio from bulk elemental analysis shows a 10-fold decreased total aluminum content compared to SP-MOR, the acid site density measured by SRS reduces over 20-fold, implying that a considerable amount of the aluminum does not contribute to the measured acidity, for example, pentahedral and octahedral aluminum species.[40]

The SRS spectra of CD_3CN in MD-MOR shows various shifts in the C≡N stretch region not only between different crystals but also within one single crystal (Figure 5A,B), depending on the extent of dealumination. In the center of a crystal, which is the least dealuminated region as shown in Figure 3B, CD_3CN chemisorbed in the main channel (I_{cc}^{SRS}) shows a shift of 10 cm^{-1} (Figure 5A), whereas the shift decreases to 2 cm^{-1} for CD_3CN in the side pocket ($I_{bb}^{SRS} - I_{cc}^{SRS}$). In the highly dealuminated regions of the crystal near the edge, the C≡N stretch of CD_3CN in the main channel decreases from 2275 to 2271 cm^{-1} (Figure 5B). Note that the relative amount of CD_3CN located in the side pockets increases in the dealuminated region (Figure 5B), implying that the acid sites in the main channel are removed preferentially (Supporting Information). The SRS spectra in the C≡N stretch region, averaged over a whole SD-MOR crystal, are shown in Figure 4C. Smaller shifts in C≡N vibration, 2 and 6 cm^{-1}, were observed for CD_3CN in the side pocket (2267 cm^{-1}, $I_{bb}^{SRS} - I_{cc}^{SRS}$) and the main channel (2271 cm^{-1}, I_{cc}^{SRS}), respectively. Despite the low intensity of the SRS signal, we estimate an approximately 5-fold increase in the relative amount of available acid sites in the side pockets *versus* main channels from the polarized SRS intensities of the measurable SD-MORs. It is known that hydrothermal dealumination produces extra-framework Al (EFAl) species, which stay in close proximity to remaining framework aluminum located mainly in the side pocket.[40,41] This change in environment (*e.g.*, in confinement effect as well as in acid site strength) can lead to the rather small peak shift observed for this situation (2 cm^{-1} with respect to liquid CD_3CN, Figure 5B); even for nitriles in bulk infrared spectroscopy, both factors have been linked to observed variations in C≡N vibration frequency.[36,42]

These spatially resolved acidity maps provide a unique insight into the dealumination process. Whereas kinetic studies of zeolite dealumination are sparse, aluminum removal is generally described to proceed *via* the reaction with an apparent first-order kinetics with respect to the total framework aluminum content;[43] this model, however, not only assumes a step-by-step aluminum removal process, which is generally accepted from bulk NMR data,[44] but also assumes homogeneous process conditions for all crystals and within every crystal's volume, such as temperature, framework composition, and the absence of chemical gradients (*e.g.*, water, dealumination agents, *etc.*).

The intercrystal heterogeneity in MD-MOR and the peculiar acid site distribution showing two distinct areas with different densities separated by a steep transition zone within individual crystals, observed for early and intermediate stage dealuminated crystals (Figure 6), cannot be explained by this hypothesis. Clearly, the extent of dealumination in the zones underneath the crystal surface where the main channels are surfacing is higher than in the middle of the crystal, suggestive of the presence of a diffusion-limited process step. Likely, a moving front, induced by hindered mass transport, is at the origin of the observed heterogeneity; the length scales over which the observed variations occur rule out temperature effects. Compositional variations are also very unlikely because of the homogeneous aluminum distribution in the starting material SP-MOR. Possibly, the EFAl species in the main channels of the mordenite strongly hinder mass transport, and the removal of these barriers and associated pore opening during acid leaching can be considered slow because of single-file diffusion. It is only upon more extensive acid leaching that fast mass transport throughout an increasingly broader outer crystal is restored. Indirect support for this hypothesis can be found in a report by Moreno and Poncelet, where the authors show a strongly reduced dealumination by acid leaching in small-port *versus* large-port mordenites, whereas variations in hydrothermal dealumination are only minimal.[30] However, it should be emphasized that mordenite dealumination is a complex process that depends on many parameters and consists of several consecutive process steps.

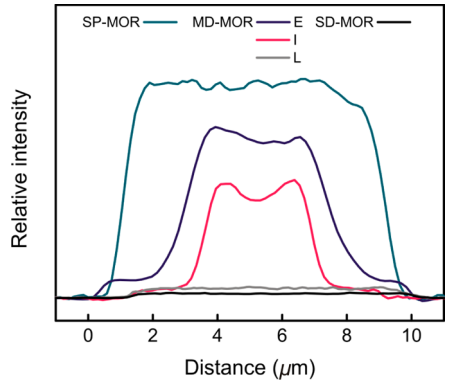

Figure 6. Horizontal line profiles of SRS signal from CD_3CN adsorbed in H-MORs. Profiles are plotted for the crystals shown in Figure 3; E, I, and L denote MD-MOR crystals at early, intermediate, and late stages of dealumination; curves are centered for better comparison.

To further support this model, benzonitrile (PhCN) was used to probe the acid site accessibility. For PhCN, an opposite trend compared to CD_3CN was found (Figure 7). SP-MOR crystals show no sign of PhCN uptake inside the crystals due to the small-port behavior. In MD-MOR samples, again three types of crystals are found. In early dealuminated crystal PhCN, probes only access the rim of the crystal just below the pore entrances, that is, the dealuminated region (Figure 7A). As the extent of dealumination increases, PhCN gradually reaches the center of the crystal, following the direction of

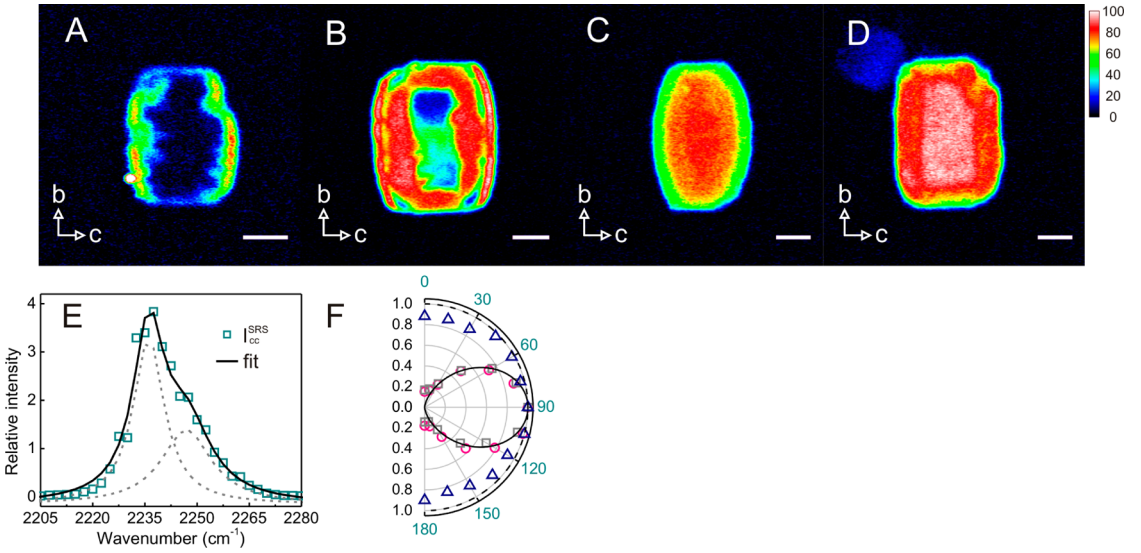

Figure 7. SRS microspectroscopy and polarization dependence of PhCN adsorbed in SP-MOR. (A–D) Chemical mapping (2249 cm^{-1}) of PhCN adsorbed in H-MORs revealing the accessibility of acid sites; gradual enhancement of acid site availability in MD-MOR from early (A), intermediate (B), and to late stages (C) of dealumination as well as SD-MOR (D). Images were recorded with lasers polarized along the crystallographic *c*-axis. False color scale indicates relative abundance of PhCN (from 0 to 100 au). Crystal axes are indicated by arrows. Scale bar: 3 μm. (E) SRS response in the C≡N stretch region for PhCN adsorbed in SD-MOR averaged over a single crystal; spectrum is fitted by a sum (solid line) of two Lorentzian curves (dashed lines). (F) Polar plots of 2237.5 (circle) and 2249 cm^{-1} (squares) vibrations with respect to crystallographic *b*-axis recorded in the *bc* plane of the crystal; a $\sin^2\theta$ function (solid line) is shown for comparison. Polar plot of 2237.5 cm^{-1} with respect to crystallographic *b*-axis recorded in the *ab* plane of the crystal (triangle); a circle with a radius of 1 (solid line) is shown for comparison.

main channels (Figure 7B). Extensive self-healing and mesopore creation in late stage dealuminated MD-MOR crystals and SD-MOR result in homogeneous PhCN distributions (Figure 7C,D), that is, full availability of acid sites. Two C≡N stretching frequencies, 2237 and 2249 cm^{-1}, are observed in both MD-MOR and SD-MOR with, respectively, 4 and 16 cm^{-1} shifts compared to liquid PhCN (Figure 7E). The spectral profile is similar for different samples; only the relative intensity of the 2249 cm^{-1} peak slightly decreases from 44% in MD-MOR to 37% in SD-MOR. The polar plots of both the vibrations at 2237 and 2249 cm^{-1} show that the C≡N bond is parallel to the crystallographic *c*-axis (Figure 7F); this is also evident from the very small polarization dependence of the SRS response when looking along the crystallographic *c*-axis (Figure 7F), indicating that PhCN molecules are inside the micropores with the C≡N bond aligned parallel to the main channel. Since PhCN is a stronger base than CD_3CN, the C≡N stretches of 2249 and 2237 cm^{-1} are assigned to the PhCN interacting Brønsted acid framework silanol groups and weaker EFAl species, respectively.[45]

Dealumination at the Single-Crystal Level. The catalytic reactivity, associated with the Brønsted acid hydroxyls as observed by NASCA microscopy, is dictated by the convolved effects of the active site distribution and the accessibility inside the catalyst porous network. In depth insight has now been generated by SRS microscopy using a suitable probe molecule that provides a detailed picture of the site distribution and accessibility of H-MOR crystals at different stages of the dealumination process.

Initially, before dealumination, the acid sites are homogeneously distributed throughout the microporous network of the SP crystals. These sites are, however, inaccessible to larger, aromatic molecules, limiting the oligomerization of furfuryl alcohol to the crystals' surface. At early stages of dealumination, only the outer regions of the crystal near the outer surface become partially accessible for aromatics due to the transition from small-port to large-port behavior while the core remains inaccessible to PhCN; this is reflected in the catalytic performance. At the intermediate stage of dealumination, the central part of the crystals also becomes partially available for PhCN, whereas the edges of the crystals are fully accessible; as a result, the local catalytic performance becomes largely determined by the local acid site density, which is higher in the center of the crystal. Finally, after extensive dealumination (*i.e.*, for the late stage dealuminated MD-MOR and SD-MOR), the crystals are fully available but have a strongly reduced acid site density, explaining the homogeneous reactivity map with a relatively lower turnover rate.

Mesoporosity and Catalytic Performance. Mesopore creation in zeolites is often beneficial because of the enhanced mass transport; it can, however, also deteriorate the shape selectivity. Polarized light excitation in NASCA microscopy allows determining the orientation of the formed catalytic reaction products (Figure 8).

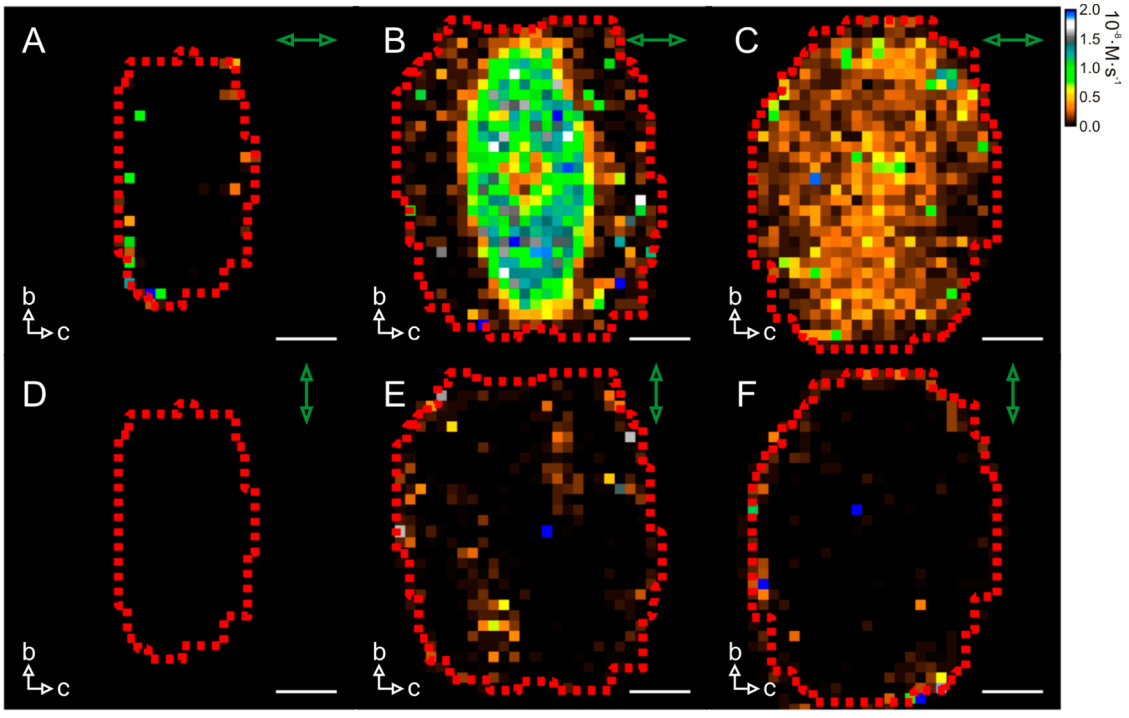

Figure 8. Polarization-resolved NASCA reactivity maps of furfuryl alcohol conversion onto H-MORs obtained for 500 × 500 × 800 nm^3 (XYZ) voxels. (A,D) SP-MOR crystal; (B,E) MD-MOR crystal; (C,F) SD-MOR crystal. Green arrow indicates orientation of polarization of excitation light; false color scale indicates observed reaction rate (from 0 to 2 × 10^{-8} M·s^{-1}); crystal axes are indicated by white arrows.

Such measurements show that over 90% of the fluorescent reaction products are aligned along the main channels for all the dealuminated mordenite samples regardless of the degree of dealumination, indicating that the acid-catalyzed furfuryl alcohol oligomerization preferentially takes place inside the original microporous structure of the mordenite crystals.

CONCLUSIONS

It has been demonstrated with NASCA microscopy that the catalytic performance of dealuminated acid mordenites shows a remarkable heterogeneity at the intercrystal and subcrystal level. Rationalization of this observation is possible by studying the acid site distribution and accessibility at the same length scales using stimulated Raman microscopy with nitrile probe molecules. Uniquely, this approach allows one to spatially resolve the acid site distribution, directly relevant to the catalytic performance rather than aluminum content, as in the case of other techniques. Importantly, the parent mordenite does not show any gradient in acid site density, and therefore, all heterogeneities observed in dealuminated samples are the result of the postsynthetic treatment. Besides stimulated Raman microspectroscopy and polarization-dependent signal intensity, the use of different nitrile probes made it possible for the first time to directly generate insights into the removal of aluminum from different framework positions as well as to unravel the complex interplay between framework aluminum removal and the small-port to large-port mordenite transition by steaming and acid leaching. Similar questions are highly relevant not only to H-MOR and the effect of dealumination but also to zeolite research in general. This novel approach can be applied to study the physicochemical properties of heterogeneous catalysts in general by adapting well-developed strategies in infrared spectroscopy.

MATERIALS AND METHODS

NASCA Microscopy[13]**.** Synthetic mordenites SP-MOR (ZM-101, NH_4 form, Si/Al ratio 6.2), MD-MOR (ZM-510, H form, Si/Al ratio 11), and SD-MOR (ZM-980, H form, Si/Al ratio 65) were obtained from Zéocat (Montoir de Bretagne, France). For the microscopy experiments, the crystals were deposited on a #1 cover glass *via* spin-coating from an aqueous suspension. Calcination on the cover glass in an ashing furnace (Nabertherm LVT 3/11) was done according to the following three-step procedure. First, the samples were heated to 80 °C (1 °C/min) and kept at this temperature for 1 h to remove easily desorbing molecules. Next, they were heated to 120 °C (1 °C/min) and kept at this temperature for 1 h to remove physisorbed water and minimize undesirable hydrothermal dealumination. Further, the samples were heated to 450 °C (1 °C/min) at which temperature the samples were kept for 50 h to remove contaminants and convert SP-MOR into the acidic H form. After this heat treatment, samples were cooled and used for microscopy experiments within several hours after cooling. Liquid-phase experiments on an inverted epifluorescence microscope were performed using a Teflon container sealed to the glass coverslip *via* a silicone rubber gasket.

Furfuryl alcohol oligomerization (water−furfuryl alcohol mixture 0.7 wt %) was used as a fluorogenic reaction for the NASCA experiments. Furfuryl alcohol (Sigma-Aldrich, 98%) was additionally purified by vacuum distillation prior to the measurements. Milli-Q water was obtained from the water purification system Synergy UV (Merck Millipore).

The NASCA investigation was performed on the wide-field setup based on an inverted microscope IX71 platform (Olympus, Japan) equipped with an oil immersion objective lens (Olympus, 100×, 1.4 NA) and a diode-pumped solid-state Excelsior laser (Spectra-Physics, USA). The latter provided a laser excitation with $\lambda_{exc} = 532$ nm (Spectra-Physics Excelsior) of 100 W/cm^2 power on the sample. Fluorescence imaging (545 nm long-pass filter) was performed with an EM-CCD camera ImagEM Enhanced C9100-13 (Hamamatsu, Japan). Further single-molecule identification, localization, and generation of the NASCA images were performed with dedicated routines (http://sushi.chem.kuleuven.be/svn/Localizer/) for IgorPro v.6.34A software (Wavemetrics, USA). The presented images were obtained by the accumulation of localized fluorescent emitters which appeared during reaction in the focal plane in the middle of the crystals for a recording duration of 90 s.

SRS Microscopy[25]**.** The mordenites were deposited on a clean cover glass #1 *via* spin-coating from an aqueous suspension. These mordenite-loaded cover glasses were heated to 450 °C with a temperature ramp of 1 °C/min under air. After 10 h at 450 °C, these samples were quickly transferred, while hot, into a cleaned desiccator under nitrogen atmosphere. After being cooled to room temperature the desiccator was opened briefly to add a few drops of liquid CD_3CN (100% with 99.96% D atom, Sigma-Aldrich) or PhCN (99%, Sigma-Aldrich) to the samples. After 10 h and prior to measurements, the excess nitrile was removed by purging with argon. The SRS imaging was performed on an upright microscope (BX61WI/FV1000, Olympus) with 25×, 1.05 NA water immersion objective (XLPLAN, Olympus). An optical parametric oscillator (OPO) (Levante Emerald, APE-Berlin) was synchronously pumped by the second harmonic of a Nd:YVO4 laser (picoTRAIN, High-Q) operating at a fundamental wavelength of 1064 nm with a repetition of 80 MHz. The OPO employs a temperature-tuned noncritically phase-matched LBO crystal and an intracavity Lyot filter to allow continuous tuning of the OPO output. The signal beam (700−980 nm) from the OPO and the fundamental 1064 nm beam were used as the pump and Stokes beam, respectively. The Stokes beam was amplitude-modulated at 9.7 MHz with a Pockel Cell (model 360-80, ConOptics) triggered by a function generator (model 29, Waveteck). The power of each beam at focus was 15−20 mW. The transmitted beams were collected with an oil immersion condenser (U-UCD8, Olympus) and were then reflected off the microscope with a dichroic mirror (FF750, Semrock). A band-pass filter (Chroma Technology, CARS 890/220 m) was used to block the Stokes beam, and the stimulated Raman loss (SRL) of the pump beam was detected by a large-area silicon PIN photodiode (S8650, Hamamatsu) with reversed bias of 60 V. The output photocurrent is low-pass-filtered (Mini-Circuits, BLP-1.9+) and demodulated by a lock-in amplifier (HF2LI, Zurich Instrument). The output of the lock-in amplifier is fed into the analog-to-digital converter (FV-10-ANALOG, Olympus) synchronized with the scanning unit. Optical transmission images were recorded with a digital camera (XC50, Olympus).

For the SRL spectra acquisition, OPO is sequentially tuned with home-built LabVIEW software. An SRL image was recorded within a fixed field of view at each OPO wavelength, that is, hyperspectral imaging, which allowed us to analyze the SRL spectra in any specific region of interest. The intensity variations of the OPO beam were recorded simultaneously by reflecting 10% of the OPO beam to a power meter with a broad-band beam splitter (FS01, Semrock) and were used to correct the SRL signal. The polarization dependence of the SRL signal was

measured by simultaneously controlling the polarization of the pump and Stokes beams with two zero-order half-wave plates (WPH05M, Thorlabs). Before recording SRL image or spectra, an analyzer was used to ensure that the polarizations of the two beams are parallel in either vertical or horizontal plane.

Conflict of Interest: The authors declare no competing financial interest.

Acknowledgment. The authors thank the "Fonds voor Wetenschappelijk Onderzoek"(Grant G0197.11), the KU Leuven Research Fund (OT/12/059), Belspo (IAP-VII/05), and the Flemish government (long term structural funding—Methusalem funding CASAS METH/08/04). M.B.J.R. acknowledges the European Research Council for financial support (ERC Starting Grant 307523). M.B.J.R. conceived the project; K.-L.L. performed the coherent Raman measurements and related analysis; A.V.K. carried out the fluorescence microscopy and NASCA analysis; all authors were involved in data interpretation and article writing.

Supporting Information Available: Detailed description of calculation procedures for analysis of NASCA and Raman microscopy data. This material is available free of charge *via* the Internet at http://pubs.acs.org.

REFERENCES AND NOTES

1. Mizuno, N.; Misono, M. Heterogeneous Catalysis. *Chem. Rev.* **1998**, *98*, 199–218.
2. Tanabe, K.; Holderich, W. F. Industrial Application of Solid Acid—Base Catalysts. *Appl. Catal., A* **1999**, *181*, 399–434.
3. Busca, G. Acid Catalysts in Industrial Hydrocarbon Chemistry. *Chem. Rev.* **2007**, *107*, 5366–5410.
4. Čejka, J.; Centi, G.; Perez-Pariente, J.; Roth, W. J. Zeolite-Based Materials for Novel Catalytic Applications: Opportunities, Perspectives and Open Problems. *Catal. Today* **2012**, *179*, 2–15.
5. Meier, W. M. The Crystal Structure of Mordenite (Ptilolite)*. *Z. Kristallogr.* **1961**, *115*, 439–450.
6. Magnoux, P.; Cartraud, P.; Mignard, S.; Guisnet, M. Coking, Aging, and Regeneration of Zeolites III. Comparison of the Deactivation Modes of H-Mordenite, HZSM-5, and HY during *n*-Heptane Cracking. *J. Catal.* **1987**, *106*, 242–250.
7. Remy, M.; Genet, M.; Notté, P.; Lardinois, P. F.; Poncelet, G. Characterization of Al Coordination at the Outer Surface of Dealuminated Mordenites by X-ray Photoelectron Spectroscopy. *Microporous Mater.* **1993**, *2*, 7–15.
8. Nesterenko, N. S.; Thibault-Starzyk, F.; Montouillout, V.; Yuschenko, V. V.; Fernandez, C.; Gilson, J.-P.; Fajula, F.; Ivanova, I. I. Accessibility of the Acid Sites in Dealuminated Small-Port Mordenites Studied by FTIR of Co-adsorbed Alkylpyridines and CO. *Microporous Mesoporous Mater.* **2004**, *71*, 157–166.
9. Roeffaers, M. B. J.; De Cremer, G.; Uji-i, H.; Muls, B.; Sels, B. F.; Jacobs, P. A.; De Schryver, F. C.; De Vos, D. E.; Hofkens, J. Single-Molecule Fluorescence Spectroscopy in (Bio)catalysis. *Proc. Natl. Acad. Sci. U.S.A.* **2007**, *104*, 12603–12609.
10. Cordes, T.; Blum, S. A. Opportunities and Challenges in Single-Molecule and Single-Particle Fluorescence Microscopy for Mechanistic Studies of Chemical Reactions. *Nat. Chem.* **2013**, *5*, 993–999.
11. Buurmans, I. L. C.; Weckhuysen, B. M. Heterogeneities of Individual Catalyst Particles in Space and Time As Monitored by Spectroscopy. *Nat. Chem.* **2012**, *4*, 873–886.
12. Roeffaers, M. B. J.; Sels, B. F.; Uji-i, H.; De Schryver, F. C.; Jacobs, P. A.; De Vos, D. E.; Hofkens, J. Spatially Resolved Observation of Crystal-Face-Dependent Catalysis by Single Turnover Counting. *Nature* **2006**, *439*, 572–575.
13. Roeffaers, M. B. J.; De Cremer, G.; Libeert, J.; Ameloot, R.; Dedecker, P.; Bons, A.-J.; Bückins, M.; Martens, J. A.; Sels, B. F.; De Vos, D. E.; *et al.* Super-resolution Reactivity Mapping of Nanostructured Catalyst Particles. *Angew. Chem., Int. Ed.* **2009**, *48*, 9285–9289.
14. Xu, W.; Kong, J. S.; Yeh, Y.-T. E.; Chen, P. Single-Molecule Nanocatalysis Reveals Heterogeneous Reaction Pathways and Catalytic Dynamics. *Nat. Mater.* **2008**, *7*, 992–996.
15. de Smit, E.; Swart, I.; Creemer, J. F.; Hoveling, G. H.; Gilles, M. K.; Tyliszczak, T.; Kooyman, P. J.; Zandbergen, H. W.; Morin, C.; Weckhuysen, B. M.; *et al.* Nanoscale Chemical Imaging of a Working Catalyst by Scanning Transmission X-ray Microscopy. *Nature* **2008**, *456*, 222–225.
16. Aramburo, L. R.; de Smit, E.; Arstad, B.; van Schooneveld, M. M.; Sommer, L.; Juhin, A.; Yokosawa, T.; Zandbergen, H. W.; Olsbye, U.; de Groot, F. M. F.; *et al.* X-ray Imaging of Zeolite Particles at the Nanoscale: Influence of Steaming on the State of Aluminum and the Methanol-to-Olefin Reaction. *Angew. Chem., Int. Ed.* **2012**, *51*, 3616–3619.
17. Aramburo, L. R.; Liu, Y.; Tyliszczak, T.; de Groot, F. M. F.; Andrews, J. C.; Weckhuysen, B. M. 3D Nanoscale Chemical Imaging of the Distribution of Aluminum Coordination Environments in Zeolites with Soft X-ray Microscopy. *ChemPhysChem* **2013**, *14*, 496–499.
18. Aramburo, L. R.; Teketel, S.; Svelle, S.; Bare, S. R.; Arstad, B.; Zandbergen, H. W.; Olsbye, U.; de Groot, F. M. F.; Weckhuysen, B. M. Interplay between Nanoscale Reactivity and Bulk Performance of H-ZSM-5 Catalysts during the Methanol-to-Hydrocarbons Reaction. *J. Catal.* **2013**, *307*, 185–193.
19. Stavitski, E.; Weckhuysen, B. M. Infrared and Raman Imaging of Heterogeneous Catalysts. *Chem. Soc. Rev.* **2010**, *39*, 4615–4625.
20. Bañares, M. A.; Mestl, G. Structural Characterization of Operating Catalysts by Raman Spectroscopy. *Adv. Catal.* **2009**, *52*, 43–128.
21. Knops-Gerrits, P.-P.; De Vos, D. E.; Feijen, E. J. P.; Jacobs, P. A. Raman Spectroscopy on Zeolites. *Microporous Mater.* **1997**, *8*, 3–17.
22. Kox, M. H. F.; Domke, K. F.; Day, J. P. R.; Rago, G.; Stavitski, E.; Bonn, M.; Weckhuysen, B. M. Label-Free Chemical Imaging of Catalytic Solids by Coherent Anti-Stokes Raman Scattering and Synchrotron-Based Infrared Microscopy. *Angew. Chem., Int. Ed.* **2009**, *48*, 8990–8994.
23. Domke, K. F.; Riemer, T. A.; Rago, G.; Parvulescu, A. N.; Bruijnincx, P. C. A.; Enejder, A.; Weckhuysen, B. M.; Bonn, M. Tracing Catalytic Conversion on Single Zeolite Crystals in 3D with Nonlinear Spectromicroscopy. *J. Am. Chem. Soc.* **2012**, *134*, 1124–1129.
24. Day, J. P. R.; Domke, K. F.; Rago, G.; Kano, H.; Hamaguchi, H.; Vartiainen, E. M.; Bonn, M. Quantitative Coherent Anti-Stokes Raman Scattering (CARS) Microscopy. *J. Phys. Chem. B* **2011**, *115*, 7713–7725.
25. Freudiger, C. W.; Min, W.; Saar, B. G.; Lu, S.; Holtom, G. R.; He, C.; Tsai, J. C.; Kang, J. X.; Xie, X. S. Label-Free Biomedical Imaging with High Sensitivity by Stimulated Raman Scattering Microscopy. *Science* **2008**, *322*, 1857–1861.
26. Zhang, X.; Roeffaers, M. B. J.; Basu, S.; Daniele, J. R.; Fu, D.; Freudiger, C. W.; Holtom, G. R.; Xie, X. S. Label-Free Live-Cell Imaging of Nucleic Acids Using Stimulated Raman Scattering Microscopy. *ChemPhysChem* **2012**, *13*, 1054–1059.
27. Freund, E.; Marcilly, C.; Raatz, F. Pore Opening of a Small-Port Mordenite by Air-Calcination. *J. Chem. Soc., Chem. Commun.* **1982**, *5*, 309.
28. Raatz, F.; Marcilly, C.; Freund, E. Comparison between Small Port and Large Port Mordenites. *Zeolites* **1985**, *5*, 329–333.
29. Van Geem, P. C.; Scholle, K. F. M. G. J.; Van der Velden, G. P. M.; Veeman, W. S. Study of the Transformation of Small-Port into Large-Port Mordenite by Magic-Angle Spinning NMR and Infrared Spectroscopy. *J. Phys. Chem.* **1988**, *92*, 1585–1589.
30. Moreno, S.; Poncelet, G. Dealumination of Small- and Large-Port Mordenites: A Comparative Study. *Microporous Mater.* **1997**, *12*, 197–222.
31. Hamon, C.; Bandiera, J.; Senes, M. Production of Hydrocarbons from Methanol in the Presence of Zeolite Catalysts. U.S. Patent 4,447,669, 1984.
32. Roeffaers, M. B. J.; Hofkens, J.; De Cremer, G.; De Schryver, F. C.; Jacobs, P. A.; De Vos, D. E.; Sels, B. F. Fluorescence Microscopy: Bridging the Phase Gap in Catalysis. *Catal. Today* **2007**, *126*, 44–53.

33. Roeffaers, M. B. J.; Ameloot, R.; Baruah, M.; Uji-i, H.; Bulut, M.; De Cremer, G.; Müller, U.; Jacobs, P. A.; Hofkens, J.; Sels, B. F.; *et al.* Morphology of Large ZSM-5 Crystals Unraveled by Fluorescence Microscopy. *J. Am. Chem. Soc.* **2008**, *130*, 5763–5772.
34. Ameloot, R.; Vermoortele, F.; Hofkens, J.; De Schryver, F. C.; De Vos, D. E.; Roeffaers, M. B. J. Three-Dimensional Visualization of Defects Formed during the Synthesis of Metal-Organic Frameworks: A Fluorescence Microscopy Study. *Angew. Chem., Int. Ed.* **2013**, *52*, 401–405.
35. Bevilacqua, M.; Alejandre, A. G.; Resini, C.; Casagrande, M.; Ramirez, J.; Busca, G. An FTIR Study of the Accessibility of the Protonic Sites of H-Mordenites. *Phys. Chem. Chem. Phys.* **2002**, *4*, 4575–4583.
36. Marie, O.; Thibault-Starzyk, F.; Lavalley, J.-C. Confirmation of the Strongest Nitriles−Hydroxy Groups Interaction in the Side Pockets of Mordenite Zeolites. *Phys. Chem. Chem. Phys.* **2000**, *2*, 5341–5349.
37. Montanari, T.; Bevilacqua, M.; Busca, G. A Study of the Localization and Accessibility of Brønsted and Lewis Acid Sites of H-Mordenite through the FT-IR Spectroscopy of Adsorbed Branched Nitriles. *Appl. Catal., A* **2006**, *307*, 21–29.
38. Dominguez-Soria, V. D.; Calaminici, P.; Goursot, A. Theoretical Study of Host−Guest Interactions in the Large and Small Cavities of MOR Zeolite Models. *J. Phys. Chem. C* **2011**, *115*, 6508–6512.
39. Huo, H.; Peng, L.; Gan, Z.; Grey, C. P. Solid-State MAS NMR Studies of Brønsted Acid Sites in Zeolite H-Mordenite. *J. Am. Chem. Soc.* **2012**, *134*, 9708–9720.
40. Chen, T.-H.; Houthoofd, K.; Grobet, P. J. Toward the Aluminum Coordination in Dealuminated Mordenite and Amorphous Silica−Alumina: A High Resolution ^{27}Al MAS and MQ MAS NMR Study. *Microporous Mesoporous Mater.* **2005**, *86*, 31–37.
41. Yu, Z.; Li, S.; Wang, Q.; Zheng, A.; Jun, X.; Chen, L.; Deng, F. Brønsted/Lewis Acid Synergy in H-ZSM-5 and H-MOR Zeolites Studied by ^{1}H and ^{27}Al DQ-MAS Solid-State NMR Spectroscopy. *J. Phys. Chem. C* **2011**, *115*, 22320–22327.
42. Smirnov, K. S.; Thibault-Starzyk, F. Confinement of Acetonitrile Molecules in Mordenite. A Computer Modeling Study. *J. Phys. Chem. B* **1999**, *103*, 8595–8601.
43. Wang, Q. L.; Gianetto, G.; Torrealba, M.; Perot, G.; Kappenstein, C.; Guisnet, M. Dealumination of Zeolites II. Kinetic Study of the Dealumination by Hydrothermal Treatment of a NH_4NaY Zeolite. *J. Catal.* **1991**, *130*, 459–470.
44. Engelhardt, G.; Lohse, U.; Patzelová, V.; Mägi, M.; Lippmaa, E. High Resolution ^{29}Si N.M.R. of Dealuminated Y-Zeolites 1. The Dependence of the Extent of Dealumination on the Degree of Ammonium Exchange and the Temperature and Water Vapour Pressure of the Thermochemical Treatment. *Zeolites* **1983**, *3*, 233–238.
45. Montanari, T.; Bevilacqua, M.; Resini, C.; Busca, G. UV−Vis and FT-IR Study of the Nature and Location of the Active Sites of Partially Exchanged Co−H Zeolites. *J. Phys. Chem. B* **2004**, *108*, 2120–2127.